Charm production in Pb+Pb collisions at the Large Hadron Collider energy

Taesoo Song,[1,2,*] Hamza Berrehrah,[1,2] Daniel Cabrera,[1,2] Wolfgang Cassing,[3] and Elena Bratkovskaya[1,2]

[1] *Institute for Theoretical Physics, Johann Wolfgang Goethe Universität, Frankfurt am Main, Germany*
[2] *Frankfurt Institute for Advanced Studies, Johann Wolfgang Goethe Universität, Frankfurt am Main, Germany*
[3] *Institut für Theoretische Physik, Universität Gießen, Germany*

We study charm production in Pb+Pb collisions at $\sqrt{s_{\rm NN}}$ =2.76 TeV in the Parton-Hadron-String-Dynamics transport approach and the charm dynamics in the partonic and hadronic medium. The charm quarks are produced through initial binary nucleon-nucleon collisions by using the PYTHIA event generator taking into account the (anti-)shadowing incorporated in the EPS09 package. The produced charm quarks interact with off-shell massive partons in the quark-gluon plasma and are hadronized into D mesons through coalescence or fragmentation close to the critical energy density, and then interact with hadrons in the final hadronic stage with scattering cross sections calculated in an effective Lagrangian approach with heavy-quark spin symmetry. The PHSD results show a reasonable $R_{\rm AA}$ and elliptic flow of D mesons in comparison to the experimental data for Pb+Pb collisions at $\sqrt{s_{NN}}$ = 2.76 TeV from the ALICE Collaboration. We also study the effect of temperature-dependent off-shell charm quarks in relativistic heavy-ion collisions. We find that the scattering cross sections are only moderately affected by off-shell charm degrees of freedom. However, the position of the peak of $R_{\rm AA}$ for D mesons depends on the strength of the scalar partonic forces which also have an impact on the D meson elliptic flow. The comparison with experimental data on the $R_{\rm AA}$ suggests that the repulsive force is weaker for off-shell charm quarks as compared to that for light quarks. Furthermore, the effects from radiative charm energy loss appear to be low compared to the collisional energy loss up to transverse momenta of $\sim$ 15 GeV/c.

PACS numbers: 25.75.Nq, 25.75.Ld

arXiv:1512.00891v2 [nucl-th] 15 Feb 2016

I. INTRODUCTION

The strong interaction, which mediates the energy-momentum exchange between hadrons as well as partons, is described by the Quantum Chromo Dynamics (QCD). The characteristic features of QCD are the asymptotic freedom at short distance and the confinement at long distance. Due to these features of QCD, the partons behave as free particle at short distance but are confined inside hadrons on distances of the order $\sim$ 1 fm. With increasing temperature or nuclear density the hadrons overlap in space, and the partons – confined before in a single hadron – now can freely move for distances that are large compared to the hadron size. The phenomenon is called deconfinement or the phase transition to a quark-gluon plasma (QGP).

Relativistic heavy-ion collisions are the experiments to realize such extreme conditions. Since the hot and dense matter produced in relativistic heavy-ion collisions disappears on time scales of a couple of fm/c, it is a big challenge to investigate its properties. One can obtain information on the system by measuring bulk particles, electromagnetic probes such as direct photons or lepton pairs or hard particles. The hard particles are normally represented by jets and heavy flavors. The former are light particles with large transverse momentum and neighbours in a momentum cone, while the latter represent heavy particles which have charm or bottom flavor. Since the production of hard particles requires large energy-momentum transfer, it takes place early in relativistic heavy-ion collisions, and can be described by perturbative QCD (pQCD).

The produced hard particle interacts with the hot dense matter by exchanging energy and momentum. For example, a hard particle with large transverse momentum (relative to the bulk matter) loses part of its energy while passing through the medium. This results in a suppression of the $R_{\rm AA}$ at high transverse momentum, which is the ratio of the measured particle number in heavy-ion collisions to the expected number in the absence of nuclear or partonic matter. With increasing strength of the interaction of a hard particle with the medium the ratio $R_{\rm AA}$ becomes more suppressed at high transverse momentum.

It has been naively expected that the $R_{\rm AA}$ of heavy flavor mesons is less suppressed as compared to that of light hadrons for two reasons: Firstly, the scattering cross section of a heavy quark is smaller in pQCD than that of a gluon which produces e.g. a light-hadron jet. Secondly, the gluon radiation from heavy quarks is suppressed due to so-called dead-cone effect [1]. However, experimental data show that the suppression of heavy-flavor mesons is comparable to that of light hadrons [2]. Also the elliptic flow of heavy-flavor hadrons is not small compared to that of light hadrons [3] and of comparable size. This sets up a puzzle for heavy-flavor production in relativistic heavy-ion collisions.

There have been various theoretical studies on the heavy-quark diffusion in relativistic heavy-ion collisions. Most of them are based on the Boltzmann equation [4–

*Electronic address: song@fias.uni-frankfurt.de

10]; an alternative way is to solve the Langevin equation [11–15] for the charm dynamics as an approximation to the Boltzmann equation. The latter again is closely linked to the Fokker-Plank equation connecting drift and diffusion by the Einstein relation at fixed temperature.

Since the heavy-flavor interaction is intimately related to the dynamics of the partonic or hadronic bulk matter, a proper description of the relativistic heavy-ion collisions is essential. The models describing the heavy-ion dynamics are classified into macroscopic and microscopic ones. Hydrodynamic simulations are a macroscopic description which assume local thermal equilibrium and numerically solve intensive thermal quantities as functions of space and time by choosing a proper Equation-of-State (EoS). There have been several attempts to include off-equilibrium effects by introducing viscosity or anisotropic momentum distributions of the hydro fluid. On the other hand, microscopic approaches are based on the Boltzmann equation or some extensions of it. For a review on the different approaches we refer the reader to Ref. [16].

The Parton-Hadron-String Dynamics (PHSD) approach, which we use in this study, differs in several aspects from the conventional Boltzmann-type approaches [17]. First of all, the degrees-of-freedom for the QGP phase are massive strongly-interacting quasiparticles. The masses of the dynamical quark and gluon in the QGP are distributed according to spectral functions whose pole positions and widths, respectively, are defined by the real and imaginary parts of their self-energies. The latter are defined in the dynamical quasiparticle model (DQPM) in which the strong coupling and the self-energies are fitted to lattice QCD results. Due to the finite spectral width, the spectral function has time-like as well as space-like parts. The time-like partons propagate in space-time within the light-cone while the space-like components are attributed to a scalar potential energy density [17]. The gradient of the potential energy density with respect to the scalar density generates a repulsive force in relativistic heavy-ion collisions and plays an essential role in reproducing experimental flow data and transverse momentum spectra. We recall that the PHSD approach has successfully described numerous experimental data in relativistic heavy-ion collisions from the Super Proton Synchrotron (SPS) to Large Hadron Collider (LHC) energies [17–20]; a review on bulk and electromagnetic properties of relativistic heavy-ion reactions within PHSD can be found in Ref. [21].

Recently, explicit charm production has been implemented in the PHSD [22]. The initial charm and anticharm quarks are produced by using the PYTHIA event generator. In the QGP they interact with off-shell partons and finally are hadronized into D mesons either through fragmentation or coalescence if the energy density is close to the critical energy density for the crossover transition (~ 0.5 GeV/fm^3). The hadronized D mesons then interact with light hadrons and finally freeze out. The PHSD approach has been applied for charm production in Au+Au collisions at $\sqrt{s_{\rm NN}}$ =200 GeV, and the results on the $R_{\rm AA}$ as well as the v_2 of D mesons are in reasonable agreement with the experimental data from the STAR collaboration [23, 24] as demonstrated in Ref. [22].

In this study we extend our previous work and apply the PHSD to charm production in Pb+Pb collisions at $\sqrt{s_{\rm NN}}$ =2.76 TeV. In this way we can examine the validity and consistency of the PHSD approach in describing charm production in relativistic heavy-ion collisions in a wide range of collision energies in connection with our previous study [22] and in connection with the dynamics of light-flavor hadrons [21]. We also study the effects of parton (anti-)shadowing and of off-shell charm and anticharm quarks on the charm production and dynamics in relativistic heavy-ion collisions at the LHC.

This paper is organized as follows: The charm production in initial nucleon-nucleon binary collisions is described in Sec. II and the results are compared with those from Fixed-Order Next-to-Leading Logarithm (FONLL) calculations and the experimental data in p+p collisions. In Sec. III, we explain how the (anti-)shadowing effect is implemented in PHSD which had been discarded in Ref. [22] at RHIC energies. We then describe the partonic and hadronic interactions of charm as well as its hadronization in Sec. IV. Finally, the nuclear modification and elliptic flow of D mesons from the PHSD are shown in Sec. V and compared with the experimental data from the ALICE collaboration. Sec. VI gives a summary of the present work.

II. INITIAL CHARM QUARK PRODUCTION

We generate initial charm and anticharm quark pairs by using the PYTHIA event generator [25]. In order to reproduce the differential cross sections for charm quark production from the Fixed-Order Next-to-Leading Logarithm (FONLL) calculations [26], the rapidity distribution of the charm quark is increased by 9 %. In Fig. 1 we compare the transverse momentum spectrum and the rapidity distribution of charm quarks in p+p collisions at $\sqrt{s_{\rm NN}}$ =2.76 TeV from the FONLL and those from the tuned PYTHIA event generator. We note that the differential cross section from the FONLL is rescaled for comparison.

The produced charm and anticharm quarks in p+p collisions hadronize by emitting soft gluons. The probabilities for a charm quark to hadronize into D^+, D^0, D_s^+, and D^{*+} are, respectively, taken to be 0.226, 0.557, 0.101, and 0.238 from the combined e^+e^- data with D^* decay into D^+ and D^0 being included [27–29]. The fraction of D^{*0} is given by multiplying to the fraction of D^{*+} the ratio of neutral to charged D meson production rate, $R_{u/d}$, which is taken to be 1.09 [29]. The three-momentum of a hadronized D meson is given by the fragmentation function [30],

$$D_Q^H(z) \sim \frac{1}{z[1-1/z-\epsilon_Q/(1-z)]^2}, \qquad (1)$$

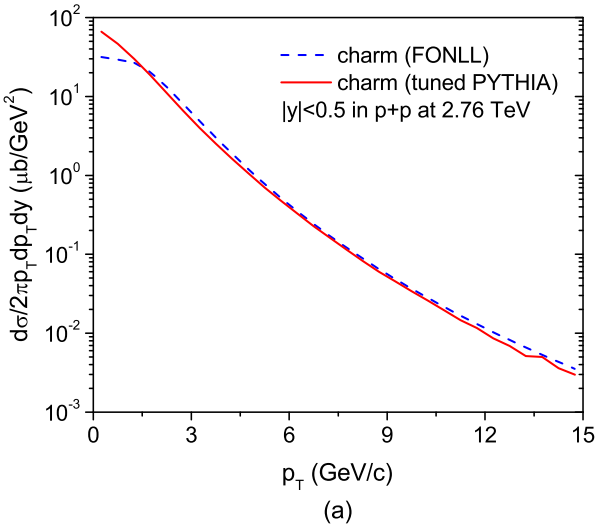

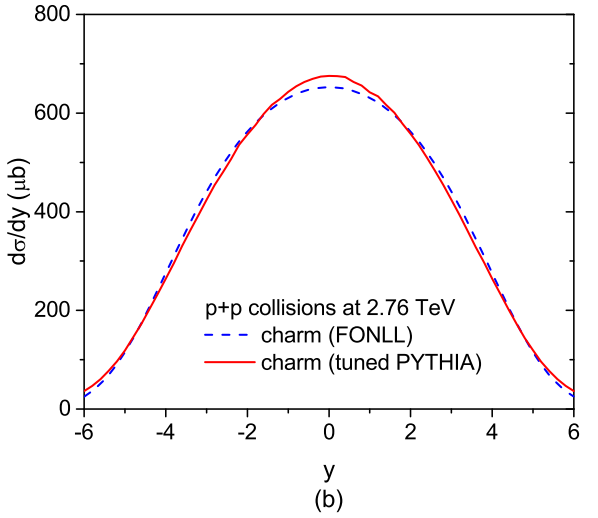

FIG. 1: (Color online) Transverse momentum (a) and rapidity (b) distributions of charm quarks in p+p collisions at $\sqrt{s_{\rm NN}}$ =2.76 TeV from FONLL (dashed lines) and the tuned PYTHIA event generator (solid lines).

where z is the momentum fraction of the hadron H fragmented from the heavy quark Q while ϵ_Q is a fit parameter which is taken to be $\epsilon_Q = 0.01$ as in our previous study [22]. The energy of the D meson is adjusted to be on mass-shell.

Fig. 2 shows the differential cross sections of D^0, D^+, and D^{*+} mesons after the charm fragmentation in p+p collisions at $\sqrt{s_{\rm NN}}$ =2.76 TeV in comparison with the experimental data from the ALICE collaboration [27]. The agreement with the experimental data is sufficiently good.

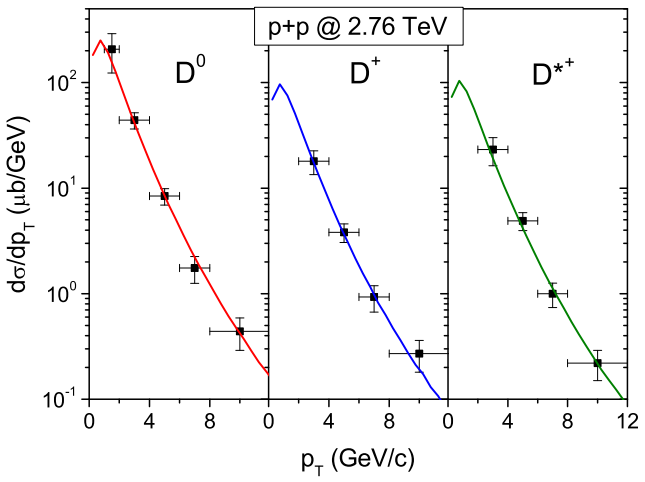

FIG. 2: (Color online) Differential cross sections for D^0, D^+, and D^{*+} production at mid-rapidity ($|y| < 0.5$) in p+p collisions at $\sqrt{s_{\rm NN}}$ =2.76 TeV from the ALICE collaboration [27] compared with those from the tuned PYTHIA event generator and the fragmentation function of Peterson [30] (solid lines).

III. (ANTI-)SHADOWING EFFECTS

In pQCD, a charm quark pair is produced through parton scattering. The partonic scattering cross section for charm production is then weighted by parton distribution functions of the nucleon in order to calculate the production cross section in nucleon-nucleon collisions:

$$\sigma_{c\bar{c}}^{NN}(s) = \sum_{i,j} \int dx_1 dx_2 f_i^N(x_1, Q) f_j^N(x_2, Q) \times \sigma_{c\bar{c}}^{ij}(x_1 x_2 s, Q), \quad (2)$$

where $f_i^N(x, Q)$ is the distribution function of the parton i with the energy-momentum fraction x in the nucleon at scale Q. The momentum fractions x_1 and x_2 are calculated from the transverse mass (M_T) and the rapidity (y) of the final-state particles by

$$x_1 = \frac{M_T}{E_{\rm cm}} e^{y}, \quad x_2 = \frac{M_T}{E_{\rm cm}} e^{-y}, \quad (3)$$

where $E_{\rm cm}$ is the nucleon-nucleon collision energy in the center-of-mass frame. We recall that a nucleon is occupied by valence quarks at large x and dominantly by gluons at small x. Since charm-quark pair production requires a large energy-momentum transfer, partons with large x dominantly contribute to the production. However, with increasing collision energy, partons with small x are more and more involved in charm pair production. As a result, gluon fusion becomes more important for

charm production than quark and antiquark annihilation for such high energy collisions as at the LHC.

Fig. 3 shows the ratio of the cross section for charm production in the channel $g+g \to c+\bar{c}$ to that in $q+\bar{q} \to c+\bar{c}$ in p+p collisions as a function of the collision energy. The partonic cross sections are calculated up to Leading-Order (LO) in pQCD [31], and the CTEQ6M parton distribution function [32] in Eq. (2). Fig. 3 shows that gluon fusion is much more important than quark and antiquark annihilation for charm pair production in high-energy collisions. Therefore, we assume in this study that all charm pairs are produced through gluon fusion.

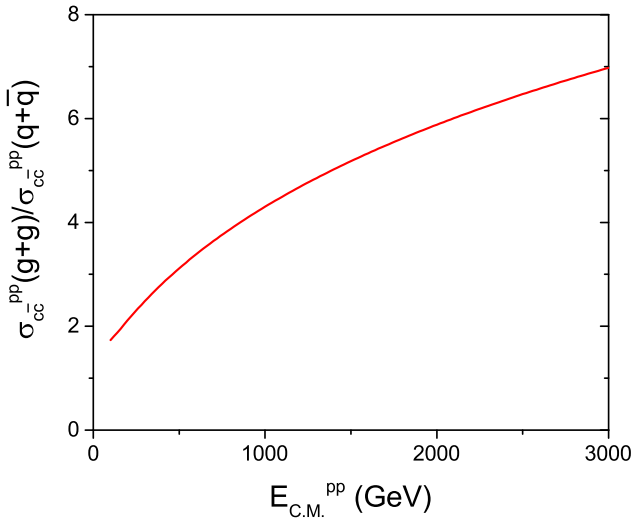

FIG. 3: (Color online) Ratio of the cross section for charm production in the channel $g+g \to c+\bar{c}$ to that in $q+\bar{q} \to c+\bar{c}$ in p+p collisions as a function of collision energy. The partonic cross sections are calculated up to LO in pQCD [31], and the CTEQ6M parton distribution function [32] is used in Eq. (2).

We recall that the parton distribution function (PDF) is modified in a nucleus to

$$f_i^{N^*}(x,Q) = R_i^A(x,Q) f_i^N(x,Q), \tag{4}$$

where N^* indicates the nucleon in nucleus A, and $R_i^A(x,Q)$ is the ratio of the PDF of N^* to that of a free nucleon. The ratio $R_i^A(x,Q)$ of a heavy nucleus A, which is lower than 1 at small x, increases with increasing x, and is slightly larger than 1 from a certain value of x. The region $R_i^A(x,Q) < 1$ is called shadowing, and the regime $R_i^A(x,Q) > 1$ is called antishadowing. The EPS09 package – used in this study – parameterizes $R_i^A(x,Q)$ from a fit of the parameters to the experimental data from deep inelastic l+A scattering, Drell-Yan dilepton production in p+A collisions, and inclusive pion production in d+Au and p+p collisions at RHIC [33].

Substituting Eq. (4) into Eq. (2), the cross section for charm production is modified to

$$\sigma_{c\bar{c}}^{N^*N^*}(s) = \sum_{i,j} \int dx_1 dx_2 R_i^A(x_1,Q) R_j^A(x_2,Q) \times f_i^N(x_1,Q) f_j^N(x_2,Q) \sigma_{c\bar{c}}^{ij}(x_1 x_2 s, Q). \tag{5}$$

In order to include the (anti-)shadowing effect in the PHSD, we take the following steps: First, the energy-momentum fractions x_1 and x_2 are calculated from the transverse mass and rapidity of the charm quark pair, which is generated by PYTHIA by using Eq. (3). Second, $R_i^A(x_1,Q)$ and $R_j^A(x_2,Q)$ for $i=j=$ gluon are obtained from the EPS09 package. The scale Q is taken to be the average of the transverse mass of the charm and that of the anticharm. Third, we introduce a maximum value of $R_i^A(x_1,Q)R_j^A(x_2,Q)$, for example, 10. If a random number is larger than the ratio of $R_i^A(x_1,Q)R_j^A(x_2,Q)$ to the maximum value, the produced charm quark pair is discarded, and a new charm quark pair is generated by PYTHIA. These steps are repeated until the random number is smaller than the ratio.

The (anti-)shadowing effect is expected to depend on the impact parameter in heavy-ion collisions such that it is strong in central collisions and weak in peripheral collisions. We assume that the (anti-)shadowing effect is proportional to the thickness of the nucleus,

$$T_A(r_\perp) = \frac{3N_A}{2\pi R_A^2} \sqrt{1 - \frac{r_\perp^2}{R_A^2}}, \tag{6}$$

where N_A and R_A are the mass number and the radius of nucleus A and $r_\perp$ is the transverse distance from the center of the nucleus. For $R_i^A(x_1,Q)$, the averaged ratio over impact parameter, we find

$$R_i^A(r_\perp,x,Q) = \frac{4}{3}\sqrt{1-\frac{r_\perp^2}{R_A^2}}\; R_i^A(x,Q), \tag{7}$$

which satisfies

$$R_i^A(x,Q) = \frac{2\pi}{N_A} \int dr_\perp r_\perp^2 T_A(r_\perp) R_i^A(r_\perp,x,Q). \tag{8}$$

The (anti-)shadowing affects the total cross section for charm production as well as the p_T spectrum of produced charm. Before taking the above steps, therefore, we pre-calculate the total cross section for each centrality from

$$\frac{\sigma_{c\bar{c}}^{N^*N^*}(s)}{\sigma_{c\bar{c}}^{NN}(s)} = \frac{1}{n}\sum_{i=1}^{n} R_g^{Pb}(r_{\perp i}^A, x_{1i}, Q_i) R_g^{Pb}(r_{\perp i}^B, x_{2i}, Q_i), \tag{9}$$

where n is the number of PYTHIA events for charm production in heavy-ion collisions, and $r_{\perp i}^A$ and $r_{\perp i}^B$, respectively, the transverse positions of the production from the center of nucleus A and nucleus B; x_{1i} and x_{2i} are calculated in each PYTHIA event by using Eq. (3).

Fig. 4 shows the ratio of differential cross section for charm production in heavy-ion collisions to that in p+p

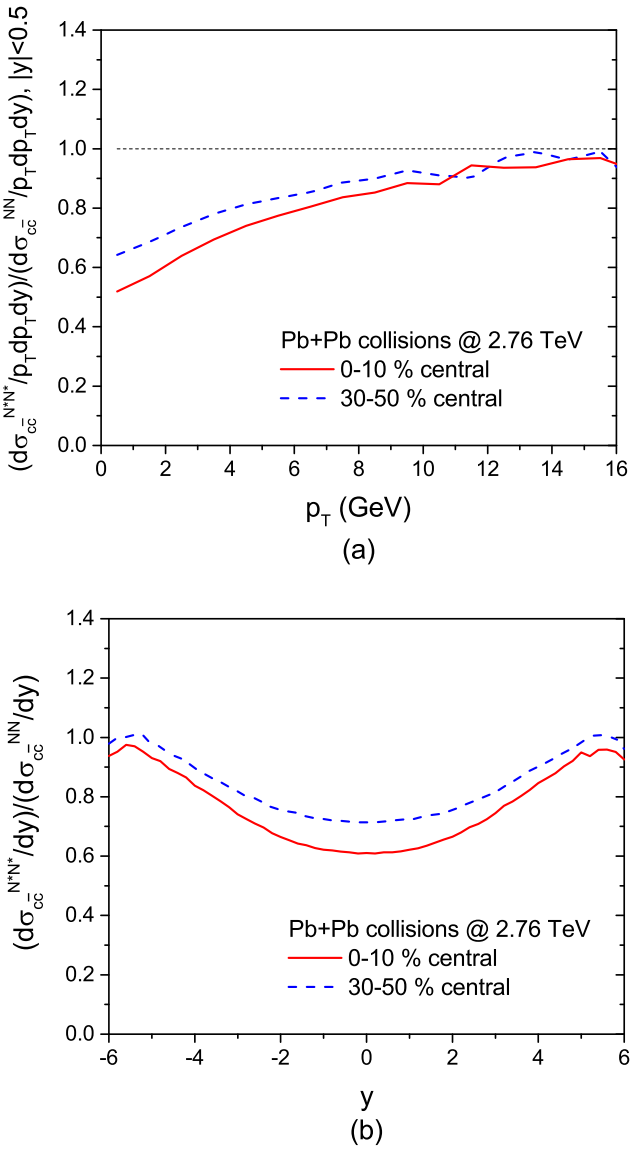

FIG. 4: (Color online) The ratio of differential cross section for charm production in heavy-ion collisions to that in p+p collisions as functions of transverse momentum p_T for $|y| < 0.5$ (a) and of rapidity (b) due to the (anti-)shadowing in 0-10 % and 30-50 % central Pb+Pb collisions at $\sqrt{s_{\rm NN}}$ =2.76 TeV.

collisions as functions of transverse momentum p_T for $|y| < 0.5$ (a) and of rapidity (b) due to (anti-)shadowing in 0-10 % and 30-50 % central Pb+Pb collisions at $\sqrt{s_{\rm NN}}$ =2.76 TeV. The production of charm and anticharm quarks is suppressed near mid-rapidity and at low transverse momentum which correspond to small x in the PDF; the suppression is larger in central collisions. Our results of shadowing effect are consistent with those from Ref. [34], because the same EPS09 package is used. However, we take into account the centrality dependence by using Eq. (7). We note that charm production is suppressed by ∼30 % in 0-10 % central collisions and by ∼ 20 % in 30-50 % central collisions.

IV. CHARM INTERACTIONS IN THE QGP

A. partonic interactions

In PHSD, baryon-baryon and baryon-meson collisions at high-energy produce strings. If the local energy density is above the critical energy density (∼ 0.5 GeV/fm^3), the strings melt into quarks and antiquarks with masses determined by the temperature-dependent spectral functions from the DQPM [35]. Massive gluons then are formed through flavor-neutral quark and antiquark fusion. In contrast to conventional elastic scattering, off-shell partons change their mass after the elastic scattering according to the local 'temperature' (energy density) in the local cell where the scattering happens. This automatically updates the parton mass distribution when the hot and dense matter expands, i.e. the local 'temperature' decreases with time.

We note that the spectral function of charm or anticharm quarks cannot be fitted from lattice QCD data because the contribution from charm or anticharm quarks to the lattice entropy is small in the temperature region of interest. Therefore, we adopt two scenarios: In the first scenario, any thermal effect on the charm quark mass is completely ignored, and the charm quark mass is 1.5 GeV regardless of temperature. In the second scenario, the temperature dependence of the pole position and width of the charm quark spectral function is exactly the same as that of light quarks apart from an increase of the charm-quark pole mass by 1.0 GeV. In the latter case, the average charm quark mass initially is ∼ 1.5 GeV, i.e. the same as in the former case. However, the charm quark, which scatters in the QGP, changes its mass according to its thermal spectral function.

Different from the usual treatment of heavy-quark scattering using the leading-order QCD perturbation theory (pQCD) [31, 36] or the inclusion of nonperturbative features in thermal perturbation theory, denoted as the hard thermal loop (HTL) approach [37], we consider all the effects of the nonperturbative nature of the strongly interacting quark-gluon plasma (sQGP) constituents, i.e. the large coupling, the multiple scattering, etc. To do so, we refrain from a fixed-order thermal loop calculation relying on perturbative self-energies (calculated in the limit of infinite temperature) to fix the in-medium masses of the quarks and gluons and pursue instead a more phenomenological approach. The multiple strong interactions of quarks and gluons in the sQGP are encoded in their effective propagators with broad spectral functions. The effective propagators, which can be interpreted as resummed propagators in a hot and dense QCD environment, have been extracted from lattice data in the scope of the DQPM [17, 38].

The leading order processes for the scattering of a heavy quark off a light quark and gluon are $qQ \to qQ$ and $gQ \to gQ$. In Refs. [38–40] we have calculated the transition matrix elements for these processes, considering the effects of finite masses and widths of the different

partons as well as the scattering angle, temperature and energy dependencies of the corresponding scattering cross sections. In this section, we highlight the differences between the two scenarios mentioned above (charm quark mass fixed at 1.5 GeV and off-shell charm quark masses) on the scattering angle, temperature and energy dependence of the cross sections as well as the charm transport coefficients.

Fig. 5 (a) shows the qQ differential elastic cross sections as a function of the scattering angle for invariant energy $\sqrt{s}$ =3 and 4 GeV, and Fig. 5 (b) the qQ total elastic cross sections as a function of center-of-mass energy. The temperature is taken to be T=0.2 GeV in the upper panel (a), and T=0.2 and T=0.3 GeV in the lower panel (b). In these figures the orange (black) lines correspond to the charm quark with a constant mass of 1.5 GeV (off-shell charm quark mass given by its DQPM spectral function). The gQ elastic cross section can be deduced from the qQ process by an appropriate Casimir color factor. Fig. 5 shows a sizeable difference between the results in the two scenarios only for large scattering angles and close to the threshold. For example, the differential cross section of off-shell charm is at most 20-25 % larger than that of charm with constant mass in backward scattering ($\cos\theta = -1$). Therefore, one can conclude that introducing off-shell masses (finite width corrections) does not change the total cross sections for heavy quark scattering on a relevant scale. This is due to the moderate parton widths for the charm quarks considered in the DQPM model. However, the two cross sections differ from each other below the threshold energy where the scattering cross section of off-shell charm quarks increases with $\sqrt{s}$, because more and more fractions of light-quark and heavy-quark spectral functions can contribute. These have peaks at the threshold energy and then decrease following the scattering cross sections of constant-mass charm quarks.

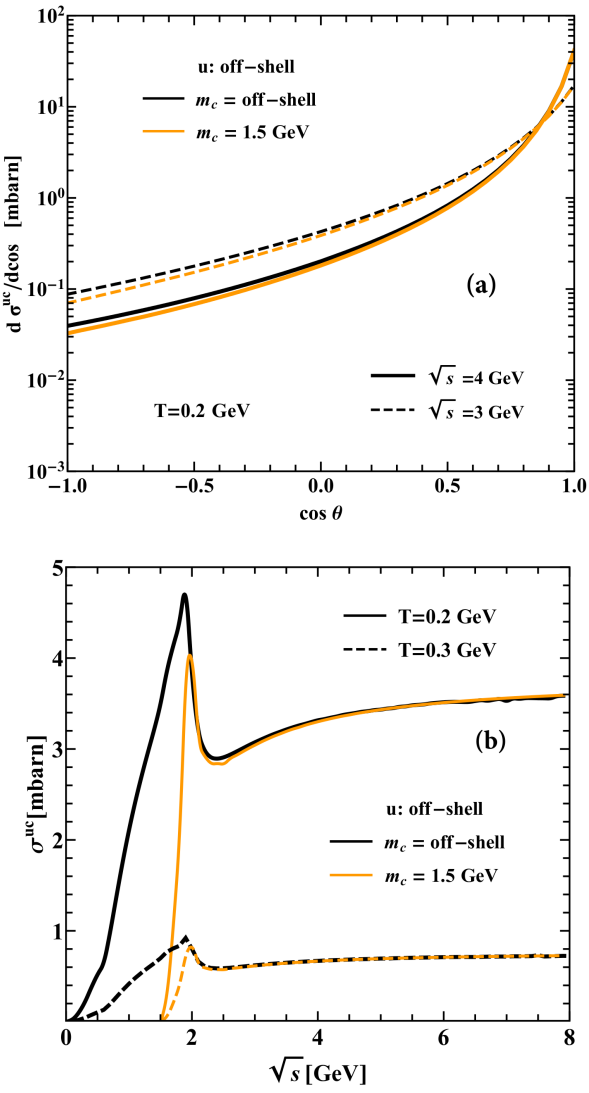

FIG. 5: (Color online) The qQ differential elastic cross sections as a function of scattering angle for invariant energy $\sqrt{s}$ = 3 and 4 GeV (a), and the qQ total elastic cross section as a function of the center-of-mass energy (b). The temperature of the QGP medium is taken to be T=0.2 GeV in the upper panel (a), and T=0.2 and T=0.3 GeV in the lower panel (b). The orange (black) lines correspond to the charm quark with a constant mass of 1.5 GeV (off-shell charm quark with a mass given by the DQPM spectral function).

The scattering of charm quarks leads to an energy and momentum loss in the hot QGP medium. The collisional energy loss of charm quark has been explicitly calculated for on- and off-shell partons in the framework of non-perturbative QCD using the partonic cross sections shown above in Refs. [39–41]. The difference between the on- and off-shell energy losses is related to the energy asymmetric contribution of the Breit-Wigner spectral function. We recall that a complex propagator is used for both scenarios, which contains an additional imaginary part proportional to the gluon width.

In Fig. 6 (a), the energy loss of charm quarks dE/dx is shown as a function of charm quark momentum for off-shell charm masses and the charm with a constant mass at T = 0.2 GeV. The energy loss of an off-shell charm is slightly smaller than that of a charm with a constant mass. The figure also shows that the heavy quark gains energy at low momentum to approach thermal equilibrium.

To validate our description of charm interactions in the QGP, the spatial diffusion constant of charm quarks D_s has been calculated on the basis of our charm scattering cross sections [39, 42, 43] and compared with that from lQCD and that of D mesons in the hadronic medium from Ref. [44]. Fig. 6 (b) shows a good agreement between our diffusion constants and those from lQCD [45] above T_c. For temperatures below T_c, we observe that the spatial diffusion constants in hadronic and partonic matter are smoothly connected and show a pronounced minimum around T_c. Finally, the diffusion constant D_s for off-shell charm is about 10 % larger than that of charm with a constant mass, because $D_s \propto \eta_D^{-1}$ and η_D is proportional

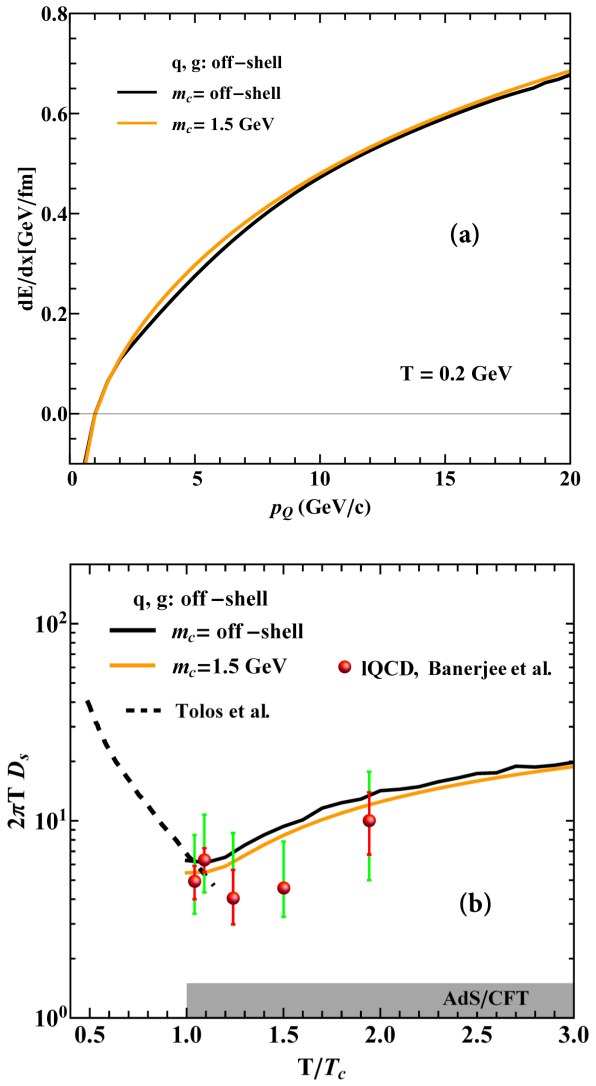

FIG. 6: (Color online) Charm collisional energy loss as a function of the charm quark momentum (a) and spatial diffusion constant D_s as a function of the medium temperature (b). The orange (black) solid lines correspond to the charm quark with a constant mass of 1.5 GeV (off-shell charm quark with a mass given by the DQPM spectral function). The black dashed line below $T = 180$ MeV is the diffusion constant of D mesons in hadronic matter from Ref. [44]. The lattice QGD calculations are taken from Ref. [45]

to the drag coefficient which quantifies the momentum and energy losses.

The comparisons in Fig. 5 and 6 show that the effect of the off-shell charm-quark mass distribution on scattering cross sections, energy loss, and spatial diffusion constant is moderate. We note that the most important factor, which decides the temperature-dependence of those quantities, is the strong coupling $g(T)$ and its infrared enhancement close to T_c which is extracted from the lattice EoS.

B. Hadronization

Once the local energy density gets lower than ∼0.75 GeV/fm^3, the charm quarks may hadronize through coalescence. In PHSD all neighboring antiquarks are candidates for the coalescence partner of the charm quark. From the distances in coordinate and momentum spaces between the charm quark and light antiquark (or vice versa), the coalescence probability is given by

$$f(\boldsymbol{\rho}, \mathbf{k}_\rho) = \frac{8 g_D}{6^2} \exp\left[-\frac{\boldsymbol{\rho}^2}{\delta^2} - \mathbf{k}_\rho^2 \delta^2\right], \qquad (10)$$

where g_D is the degeneracy of the D meson, and

$$\boldsymbol{\rho} = \frac{1}{\sqrt{2}}(\mathbf{r}_1 - \mathbf{r}_2), \quad \mathbf{k}_\rho = \sqrt{2}\,\frac{m_2 \mathbf{k}_1 - m_1 \mathbf{k}_2}{m_1 + m_2}, \qquad (11)$$

with m_i, $\mathbf{r}_i$ and $\mathbf{k}_i$ being the mass, position and momentum of the quark or antiquark i in the center-of-mass frame, respectively. The width parameter δ is related to the root-mean-square radius of the produced D meson through

$$\langle r^2 \rangle = \frac{3}{2}\frac{m_1^2 + m_2^2}{(m_1 + m_2)^2}\delta^2. \qquad (12)$$

Since this prescription gives a larger coalescence probability at low transverse momentum, the radius is taken to be 0.9 fm as in our previous study [22]. We also include the coalescence into highly excited states, $D_0^*(2400)^0$, $D_1(2420)^0$, and $D_2^*(2460)^{0,\pm}$, which are assumed to immediately decay to D or D^* and π after hadronization [22].

Summing up the coalescence probabilities from all candidates, whether the charm or anticharm quark hadronizes by coalescence or not, and which quark or antiquark among the candidates will be the coalescence partner is decided by Monte Carlo. If a random number is above the sum of the coalescence probabilities, it is tried again in the next time step till the local energy density is lower than 0.4 GeV/fm^3. The charm or anticharm quark, which does not succeed to hadronize by coalescence, then hadronizes through fragmentation as in p+p collisions.

Fig. 7 shows the coalescence probabilities of midrapidity charm ($|y| < 0.5$) as a function of the transverse momentum in 0-10 % and 30-50 % central Pb+Pb collisions at $\sqrt{s_{\rm NN}}$ =2.76 TeV. Since the charm or anticharm quark with large transverse momentum has a reduced chance to find a coalescence partner close by in phase space, the coalescence probability decreases with increasing transverse momentum. Compared with the coalescence probabilities in Au+Au collisions at 200 GeV [22], the present coalescence probabilities are slightly smaller at $p_T = 0$ and are shifted to higher p_T essentially due to the stronger transverse flow.

Since the hadronization of charm quarks through fragmentation is not properly suited at low transverse momentum, several studies have forced the coalescence

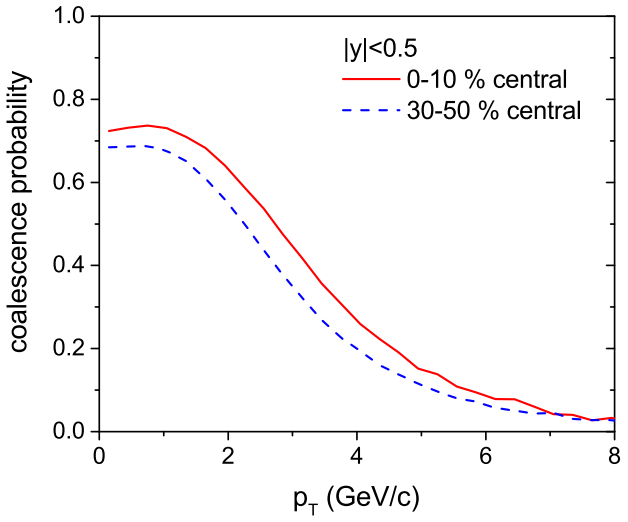

FIG. 7: (Color online) Coalescence probabilities of mid-rapidity charm ($|y| < 0.5$) as a function of the transverse momentum in 0-10 % and 30-50 % central Pb+Pb collisions at $\sqrt{s_{\rm NN}}$ =2.76 TeV.

probability to be 1 at p_T =0 [9, 12, 46, 47]. However, it is not clear presently how to control this modeling in practice. In the case of a hydrodynamic background, for example, the coalescence probability is precalculated in the thermalized matter and rescaled such that it is 1 at p_T =0 as in Refs. [9, 46]. It is no longer 1 any more after including flow effects due to the Lorentz boost. Thus is forced to be 1 at p_T =0 for each flow velocity in Ref. [46]. In the case of Boltzmann-type simulations, the coalescence probability depends on the system size, in other words, collision energy as well as centrality [22]. Although the coalescence probability may be rescaled at one collision energy and in a single centrality, the probability is not 1 at p_T =0 at other collision energies or other centralities.

We mention that it is more consistent to perform the coalescence without any additional modeling and allow a partial fragmentation at low p_T for the following reason: Though the coalescence is a promising model for the hadronization of low-p_T particles, it is barely applicable in p+p collisions. For that reason, all charm quarks are assumed to be hadronized by fragmentation in p+p collisions in Sec. II. Since the fragmentation is already allowed at low-p_T in p+p collision, which is the reference for the nuclear modifications in heavy-ion collision, there is no reason to prohibit fully the fragmentation in heavy-ion collisions. Moreover, if the fragmentation is prohibited, in other words, the coalescence probability is forced to be 1 in peripheral heavy-ion collisions, it will induce a large nuclear modification factor, although a small nuclear matter effect is expected in peripheral collisions. Therefore, we allow a partial fragmentation at low p_T, unless a better way of hadronization is adopted in p+p collisions.

Finally, we assume that the hadronization time of a charm quark is 0.5 fm/c in the rest frame, and that the charm quark does not scatter during the hadronization. The details on the hadronization time of heavy flavor are discussed in Ref. [48].

C. Hadronic interactions

The hadronized D and D^* mesons then interact with hadrons in the hadron gas phase. The cross sections for D or D^* scattering off pseudoscalar mesons (π, K, $\bar{K}$, η), baryons (N, Δ), and antibaryons ($\bar{N}$, $\bar{\Delta}$) are calculated on the basis of effective hadronic models which incorporate chiral symmetry breaking in the light-flavor sector. The additional freedom stemming from the coupling to heavy-flavored mesons is constrained by imposing heavy-quark spin symmetry (HQSS) [44, 49–55]. It has been shown that these cross sections have a non-trivial energy, isospin, and flavor dependence due to the presence of resonant states close to threshold energies with dominant decay modes involving open-charm mesons and light hadrons [22], such as the $D_0^*(2400)$ and the $D_s^*(2317)$ in $D\pi$ and DK scattering, respectively, or the $\Lambda_c(2595)$ in DN scattering, all of them dynamically generated in these approaches. The cross sections for scattering off other light hadrons (such as the vector mesons from the octet), which are not calculated above, are taken to be 10 mb and independent of the collision energy.

V. RESULTS

The medium effect on charm production in relativistic heavy-ion collisions is expressed in term of the ratio $R_{\rm AA}$, which is defined as

$$R_{\rm AA}(p_T) \equiv \frac{dN_D^{\rm Pb+Pb}/dp_T}{N_{\rm binary}^{\rm Pb+Pb} \times dN_D^{\rm p+p}/dp_T}, \qquad (13)$$

where $N_D^{\rm Pb+Pb}$ and $N_D^{\rm p+p}$ are, respectively, the numbers of D mesons produced in Pb+Pb collisions and in p+p collisions, and $N_{\rm binary}^{\rm Pb+Pb}$ is the number of binary nucleon-nucleon collisions in Pb+Pb collisions for the centrality class considered. $R_{\rm AA}$ larger (smaller) than 1.0 indicates that nuclear matter enhances (suppresses) charm production in relativistic heavy-ion collisions.

Fig. 8 shows the ratio $R_{\rm AA}$ of D^0, D^+, and D^{*+} mesons within the rapidity range $|y| < 0.5$ as a function of p_T in 0-10 % and 30-50 % central Pb+Pb collisions at $\sqrt{s_{\rm NN}}$ =2.76 TeV. Here the charm quark mass is taken to be 1.5 GeV, independent of temperature. The solid and dotted lines are, respectively, the $R_{\rm AA}$ of D mesons with and without (anti-)shadowing. We can see that the $R_{\rm AA}$ of D mesons decreases especially at small transverse momentum due to shadowing, which is consistent with Fig. 4. When including shadowing our results are

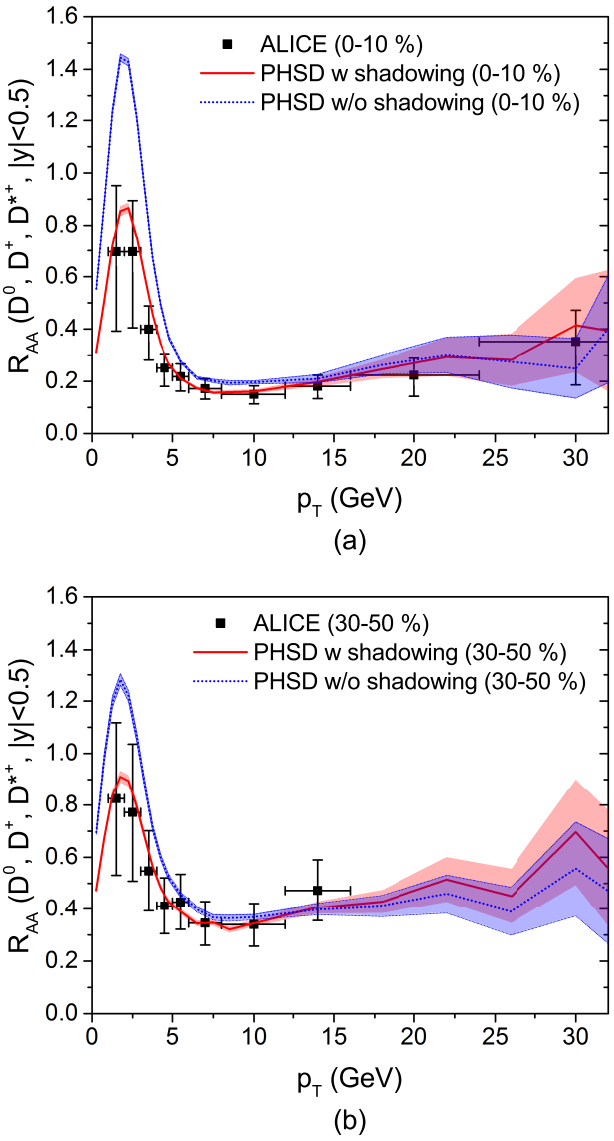

FIG. 8: (Color online) The ratio $R_{\rm AA}$ of D^0, D^+, and D^{*+} mesons within $|y| < 0.5$ as a function of p_T in 0-10 % (a) and 30-50 % (b) central Pb+Pb collisions at $\sqrt{s_{\rm NN}}$ =2.76 TeV compared with the experimental data from the ALICE collaboration [56]. The solid and dotted lines are, respectively, $R_{\rm AA}$ with and without (anti-)shadowing. The charm quark mass is taken to be 1.5 GeV.

in a good agreement with the experimental data from the ALICE collaboration [56]. Since the radiative energy loss is not yet included in our study, it seems that the latter is not significant for transverse momenta up to 15 GeV/c. At higher transverse momenta our statistics is too low to allow for a solid answer. We speculate that the dominance of partonic scattering is due to the fact that in PHSD the scattering partners of the charm quarks are massive partons.

The elliptic flow is generated in non-central heavy-ion collisions due to asymmetric pressure gradients in the transverse plane, and expressed in term of the coefficient v_2 defined as

$$v_2(p_T) \equiv \frac{\int d\phi \cos 2\phi (dN_D^{\rm Pb+Pb}/dp_T d\phi)}{dN_D^{\rm Pb+Pb}/dp_T}, \qquad (14)$$

where ϕ is the azimuthal angle of the D meson in momentum space.

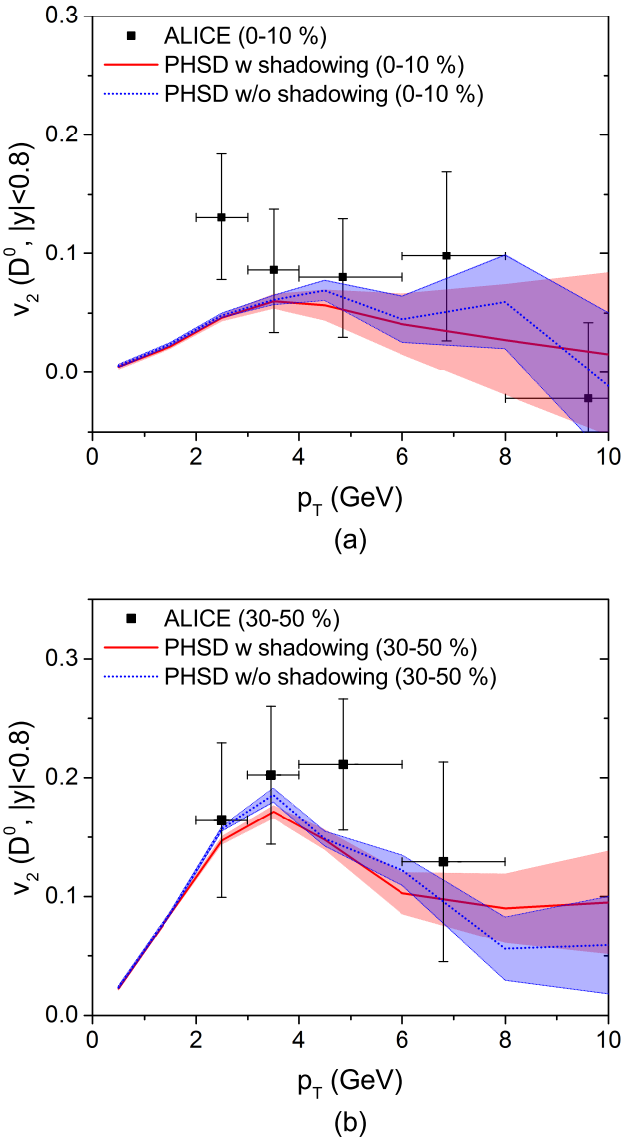

FIG. 9: (Color online) The elliptic flow v_2 of D^0 mesons within $|y| < 0.8$ in 0-10 % (a) and 30-50 % (b) central Pb+Pb collisions at $\sqrt{s_{\rm NN}}$ =2.76 TeV compared with the experimental data from the ALICE collaboration [57]. The solid and dotted lines are, respectively, v_2 with and without (anti-)shadowing. The charm quark mass is taken to be 1.5 GeV.

Fig. 9 shows the elliptic flows v_2 of D^0 mesons within the rapidity range $|y| < 0.8$ in 0-10 % and 30-50 % central Pb+Pb collisions at $\sqrt{s_{\rm NN}}$ =2.76 TeV. The solid and dotted lines are, respectively, the results with and without (anti-)shadowing. Again the charm quark mass is

taken to be 1.5 GeV. We can see that the PHSD results reproduce the experimental data from the ALICE collaboration [57]. The (anti-)shadowing effect slightly decreases the elliptic flows, because it reduces the production of low-p_T charm which more easily follows the bulk flow. It has been a challenge for theoretical models to reproduce the experimental data and to explain simultaneously the large energy loss of charm quarks (R_{AA}) and the strong collectivity (v_2) [16]. According to a recent study [58], both R_{AA} and v_2 are well reproduced if the drag coefficient for charm quarks is large close to the critical temperature. For our drag coefficient this is the case, since the strong coupling fitted to the lattice EoS rapidly increases near the critical temperature.

We point out that – for the same scattering cross sections and hadronization processes – our results are in good agreement with the experimental data in Au+Au collisions at $\sqrt{s_{NN}}$ =200 GeV as well as in Pb+Pb collisions at $\sqrt{s_{NN}}$ =2.76 TeV, which spans more than one order of magnitude in collision energy $\sqrt{s}$. Considering that the PHSD transport approach provides good bulk dynamics from SPS to LHC energies [21], our description of charm production and charm interactions in relativistic heavy-ion collisions appears consistent.

Finally, we study the effect of off-shell charm on the charm production and propagation in relativistic heavy-ion collisions. We recall that the spectral function with a finite width has both time-like and space-like parts [17]. The time-like parton propagates in space-time while the space-like one is interpreted as a virtual parton which mediates the interaction between time-like partons. The latter contributes to the potential energy density in the QGP [17]. The potential energy density is then separated into scalar and (time-component) vector parts by using the energy density and pressure of the lattice EoS [17]. At RHIC and LHC energies the scalar potential dominates by far due to approximately equal densities of quarks and antiquarks. The scalar potential energy density increases with increasing temperature (or scalar parton density) except near T_c [17], and thus gives a repulsive force on partons in relativistic heavy-ion collisions (except close to T_c or during hadronization). The repulsive force for gluons is roughly twice stronger than that for quarks or antiquarks, because one gluon is roughly equivalent to a quark and antiquark pair. It is presently not clear how much a charm quark is affected by scalar partonic forces.

Fig. 10 shows the ratio R_{AA} of D^0, D^+, and D^{*+} mesons within $|y| < 0.5$ (a) and the elliptic flow v_2 of D^0 mesons within $|y| < 0.8$ (b) as a function of p_T in 0-10 % central Pb+Pb collisions at $\sqrt{s_{NN}}$ =2.76 TeV. The solid, dashed and dotted lines are, respectively, for charm quarks with the mass of 1.5 GeV, and for off-shell charm quarks without and with the repulsive force originating from the scalar potential energy density. We note that (Anti-)shadowing is included in all cases. The comparison between the solid and dashed lines shows that the effect of off-shell charm without repulsive force on R_{AA} and v_2 is small, which is expected from Figs. 5 and 6.

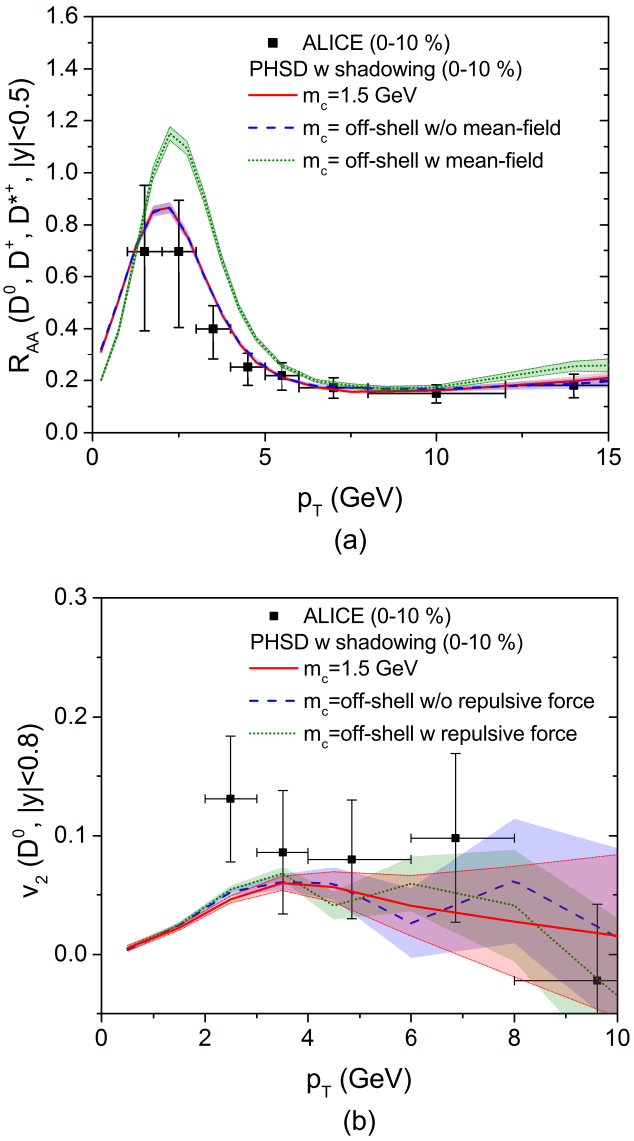

FIG. 10: (Color online) The ratio R_{AA} of D^0, D^+, and D^{*+} mesons within $|y| < 0.5$ (a) and the elliptic flow v_2 of D^0 mesons within $|y| < 0.8$ (b) as a function of p_T in 0-10 % central Pb+Pb collisions at $\sqrt{s_{NN}}$ =2.76 TeV compared with the experimental data from the ALICE collaboration [56]. The solid, dashed and dotted lines are, respectively, for charm quarks with the mass of 1.5 GeV, and for off-shell charm quarks without and with the repulsive force originated from the scalar potential energy density for light quarks. (Anti-)shadowing is included in all cases.

When including the repulsive force, the peak of the ratio R_{AA} is shifted to larger transverse momentum, as shown by the dotted lines. However, the comparison with the experimental data from the ALICE collaboration favors a weaker repulsive force for off-shell charm quarks compared to light quarks.

Fig. 11 shows the distributions of charm quark scattering in the QGP as a function of collision energy for the

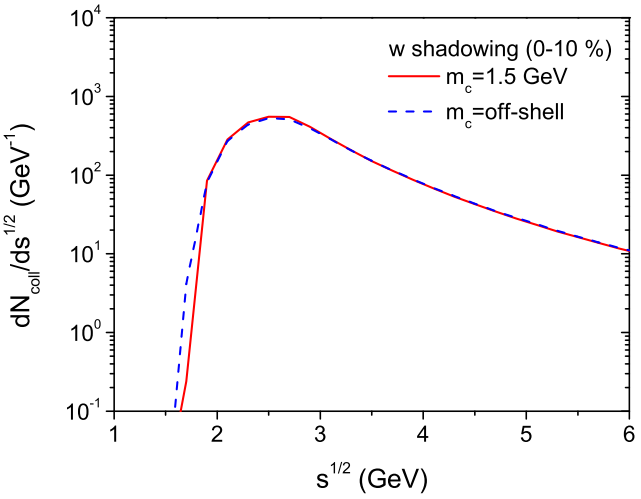

FIG. 11: (Color online) the distributions of charm quark scattering in QGP as functions of collision energy for the constant mass and the off-shell mass of charm quark in 0-10 % central Pb+Pb collisions at 2.76 TeV with the shadowing effect included.

constant mass and the off-shell mass of charm quarks in 0-10 % central Pb+Pb collisions at 2.76 TeV (with the shadowing effect included). The scattering distributions are similar to each other except at very low $\sqrt{s}$ where the number of scatterings is larger in the case of off-shell charm. As shown in Fig. 5 (b), off-shell charm has a sizeable scattering cross sections even below $\sqrt{s} = 1.5$ GeV. However, it induces only little additional scatterings because the mass of the charm quark – involved in such scatterings – is much smaller than the pole position of the charm spectral function and occurs with low probability. Considering that the number of produced charm quarks is about 84 and the total number of charm quark scattering 720 in 0-10 % centrality, one charm quark experiences on average 9 elastic scatterings before hadronization in central collisions.

VI. SUMMARY

We have studied charm production in Pb+Pb collisions at $\sqrt{s_{\rm NN}}$ =2.76 TeV in the PHSD transport approach in continuation of our calculations for Au+Au collsions at the top RHIC energy [22]. The initial charm quark pairs are produced through nucleon-nucleon binary collisions by using the PYTHIA event generator. The (anti-)shadowing, which is a modification of the parton distributions in a nucleus, has been implemented in the PHSD by using the EPS09 package. We have found that (anti-)shadowing reduces the charm quark production preferentially at low transverse momentum and at mid-rapidity.

The produced charm and anticharm quarks interact in the QGP with quarks and gluons whose masses are given by spectral functions with pole positions and widths being fitted to the lattice QCD equation-of-state (EoS) [21]. Since the contribution from charm quarks to the energy density and pressure of the QGP is small, the spectral function of a charm quark cannot be constrained by the lattice EoS. Therefore, we have studied two different scenarios: In the first case the charm quark mass is 1.5 GeV independent of temperature, i.e. the charm quark spectral function is a delta function peaked at 1.5 GeV. In the second case, the pole position and width of the charm spectral function are assumed to have the same temperature-dependence as those of light quarks except that the pole position is shifted by 1 GeV from the pole position of a light quark. We have pointed out that our partonic cross sections reproduce the spatial diffusion constant of heavy quarks from lQCD and smoothly join with that of D mesons in a hadron gas close to the critical temperature T_c.

Once the local energy density gets lower than the critical value of the crossover transition in the expansion of the system, the charm quark is hadronized into a D meson (or its excited states) through either coalescence or fragmentation. The coalescence probability of a charm quark is calculated from the light antiquarks close in coordinate and momentum space. Accordingly, a charm quark with a small transverse momentum has a large coalescence probability, while the one with a large transverse momentum has a small probability. If coalescence is rejected in the Monte-Carlo method, the charm quark is hadronized through fragmentation as in p+p reactions. The essential difference between coalescence and fragmentation is that a charm quark gains transverse momentum in the first case while it loses transverse momentum in the second one.

The hadronized D mesons then interact with hadrons in the hadron gas phase. The cross sections for D or D^* meson scattering off light pseudoscalar mesons, light baryons and antibaryons are calculated in an effective Lagrangian approach with heavy-quark spin symmetry. After several hundred fm/c, depending on collision centrality, the D mesons freeze out, and are analyzed in momentum for the comparison with experimental data.

As a result from PHSD, both the $R_{\rm AA}$ and the elliptic flow v_2 of D mesons from the ALICE collaboration are reasonably reproduced. This supports the validity and consistency of the PHSD approach for charm production and propagation in relativistic heavy-ion collisions in connection with our previous study at the top RHIC energy within the same approach [22].

Furthermore, we have found that the shadowing effect suppresses charm production preferentially at small transverse momentum and mid-rapidity, and it helps the PHSD to reproduce the ratio $R_{\rm AA}$ of D mesons from the ALICE collaboration. The shadowing also slightly decreases the elliptic flow of D mesons because it suppresses the production of charm quarks with small transverse momentum which more easily follow the bulk flow.

Finally, we have studied the effect of off-shell charm on the charm production and propagation in relativistic heavy-ion collisions. It has been found that the scattering cross sections are only moderately affected by the off-shell charm quarks, but the repulsive force – generated by a scalar potential energy – shifts the peak of $R_{\rm AA}$ of D mesons to higher transverse momentum when assuming the same strength as for the light quarks. The comparison with the experimental data on the ratio $R_{\rm AA}$ of D mesons with the actual data from the ALICE collaboration supports a weaker repulsive force for off-shell charm quarks than for the off-shell light quarks.

PHSD is a microscopic transport model that allows for the detailed study of the charm dynamics in hot and dense QCD matter within a non-equilibrium transport setting. The specific non-equilibrium features of the PHSD model sets it apart from other theoretical approaches which assume thermal equilibrium. Our future study, which compares and contrasts the results from PHSD with those from other approaches, should give an insight into the effect of non-equilibrium matter on the production and interactions of heavy flavor in relativistic heavy-ion collisions.

Acknowledgements

The authors acknowledge inspiring discussions with J. Aichelin, P. B. Gossiaux, C. M. Ko, O. Linnyk, J. Torres-Rincon, L. Tolos, V. Ozvenchuk, and R. Vogt. This work was supported by DFG under contract BR 4000/3-1 and by the LOEWE center "HIC for FAIR". The computational resources have been provided by the LOEWE-CSC.

[1] Y. L. Dokshitzer and D. E. Kharzeev, Phys. Lett. B **519**, 199 (2001).
[2] B. Abelev *et al.* [ALICE Collaboration], JHEP **1209**, 112 (2012).
[3] B. Abelev *et al.* [ALICE Collaboration], Phys. Rev. Lett. **111**, 102301 (2013).
[4] D. Molnar, Eur. Phys. J. C **49**, 181 (2007).
[5] B. Zhang, L. W. Chen and C. M. Ko, Phys. Rev. C **72**, 024906 (2005).
[6] O. Linnyk, E. L. Bratkovskaya and W. Cassing, Int. J. Mod. Phys. E **17**, 1367 (2008).
[7] J. Uphoff, O. Fochler, Z. Xu and C. Greiner, Phys. Rev. C **84**, 024908 (2011).
[8] J. Uphoff, O. Fochler, Z. Xu and C. Greiner, Phys. Lett. B **717**, 430 (2012).
[9] P. B. Gossiaux, J. Aichelin, T. Gousset and V. Guiho, J. Phys. G **37**, 094019 (2010).
[10] M. Nahrgang, J. Aichelin, P. B. Gossiaux and K. Werner, Phys. Rev. C **90**, 024907 (2014).
[11] G. D. Moore and D. Teaney, Phys. Rev. C **71**, 064904 (2005).
[12] M. He, R. J. Fries and R. Rapp, Phys. Rev. C **86**, 014903 (2012).
[13] M. He, R. J. Fries and R. Rapp, Phys. Rev. Lett. **110**, 112301 (2013).
[14] S. Cao and S. A. Bass, Phys. Rev. C **84**, 064902 (2011).
[15] S. Cao, arXiv:1511.04477 [nucl-th].
[16] A. Andronic *et al.*, arXiv:1506.03981 [nucl-ex].
[17] W. Cassing and E. L. Bratkovskaya, Nucl. Phys. A **831**, 215 (2009).
[18] E. L. Bratkovskaya, W. Cassing, V. P. Konchakovski and O. Linnyk, Nucl. Phys. A **856**, 162 (2011).
[19] V. P. Konchakovski *et al.*, J. Phys. G **42**, 055106 (2015); J. Phys. G **41**, 105004 (2014); Phys. Rev. C **90**, 014903 (2014); Phys. Rev. C **85**, 044922 (2012); Phys. Rev. C **85**, 011902 (2012).
[20] O. Linnyk *et al.*, Phys. Rev. C **92**, 054914 (2015); Phys. Rev. C **89**, 034908 (2014); Phys. Rev. C **88**, 034904 (2013); Phys. Rev. C **87**, 014905 (2013); Phys. Rev. C **85**, 024910 (2012); Phys. Rev. C **84**, 054917 (2011); Nucl. Phys. A **855**, 273 (2011).
[21] O. Linnyk, E. L. Bratkovskaya, and W. Cassing, Prog. Part. Nucl. Phys. **87**, 50 (2016).
[22] T. Song, H. Berrehrah, D. Cabrera, J. M. Torres-Rincon, L. Tolos, W. Cassing and E. Bratkovskaya, Phys. Rev. C **92**, 014910 (2015).
[23] L. Adamczyk *et al.* [STAR Collaboration], Phys. Rev. Lett. **113**, 142301 (2014).
[24] D. Tlusty [STAR Collaboration], Nucl. Phys. A **904-905**, 639c (2013).
[25] T. Sjostrand, S. Mrenna and P. Z. Skands, JHEP **0605**, 026 (2006).
[26] M. Cacciari, S. Frixione, N. Houdeau, M. L. Mangano, P. Nason and G. Ridolfi, JHEP **1210**, 137 (2012).
[27] B. Abelev *et al.* [ALICE Collaboration], JHEP **1207**, 191 (2012).
[28] L. Gladilin, hep-ex/9912064.
[29] S. Chekanov *et al.* [ZEUS Collaboration], JHEP **0707**, 074 (2007).
[30] C. Peterson, D. Schlatter, I. Schmitt and P. M. Zerwas, Phys. Rev. D **27**, 105 (1983).
[31] B. L. Combridge, Nucl. Phys. B **151**, 429 (1979).
[32] J. Pumplin, D. R. Stump, J. Huston, H. L. Lai, P. M. Nadolsky and W. K. Tung, JHEP **0207**, 012 (2002).
[33] K. J. Eskola, H. Paukkunen and C. A. Salgado, JHEP **0904**, 065 (2009).
[34] S. Cao, G. Y. Qin and S. A. Bass, Phys. Rev. C **92**, no. 2, 024907 (2015).
[35] W. Cassing, Eur. Phys. J. ST **168**, 3 (2009); Nucl. Phys. A **795**, 70 (2007).
[36] R. Cutler and D. Sivers, Phys. Rev. D 17, 196 (1978).
[37] E. Braaten and M. H. Thoma, Phys. Rev. D 44, 1298 (1991); A. Peshier, Nucl. Phys. A 888, 7 (2012); S. Peigne and A. Peshier, Phys. Rev. D 77, 114017 (2008); P. B. Gossiaux and J. Aichelin, Phys. Rev. C 78, 014904 (2008); P. B. Gossiaux, R. Bierkandt, and J. Aichelin, Phys. Rev. C 79, 044906 (2009).
[38] H. Berrehrah, E. Bratkovskaya, W. Cassing, P. B. Gossiaux, J. Aichelin and M. Bleicher, Phys. Rev. C **89**,

054901 (2014).
[39] H. Berrehrah, P. B. Gossiaux, J. Aichelin, W. Cassing and E. Bratkovskaya, Phys. Rev. C **90**, 064906 (2014).
[40] H. Berrehrah, E. Bratkovskaya, W. Cassing, P. B. Gossiaux and J. Aichelin, Phys. Rev. C **91**, 054902 (2015).
[41] H. Berrehrah, E. Bratkovskaya, W. Cassing, P. B. Gossiaux and J. Aichelin, J. Phys. Conf. Ser. **509**, 012076 (2014).
[42] H. Berrehrah, P.B. Gossiaux, J. Aichelin, W. Cassing, J.M. Torres-Rincon, and E. Bratkovskaya, Phys. Rev. C **90**, 051901 (2014).
[43] H. Berrehrah, E. Bratkovskaya, W. Cassing and R. Marty, J. Phys. Conf. Ser. **612**, 012050 (2015).
[44] L. Tolos and J. M. Torres-Rincon, Phys. Rev. D **88**, 074019 (2013).
[45] D. Banerjee *et al.* , Phys. Rev. D **85**, 014510 (2012).
[46] S. Cao, G. Y. Qin and S. A. Bass, Phys. Rev. C **88**, 044907 (2013).
[47] Y. Oh, C. M. Ko, S. H. Lee and S. Yasui, Phys. Rev. C **79**, 044905 (2009).
[48] T. Song and H. Berrehrah, arXiv:1601.04449 [nucl-th].
[49] L. M. Abreu, D. Cabrera, F. J. Llanes-Estrada and J. M. Torres-Rincon, Annals Phys. **326**, 2737 (2011).
[50] L. M. Abreu, D. Cabrera and J. M. Torres-Rincon, Phys. Rev. D **87**, 034019 (2013).
[51] C. Garcia-Recio, V. K. Magas, T. Mizutani, J. Nieves, A. Ramos, L. L. Salcedo and L. Tolos, Phys. Rev. D **79**, 054004 (2009).
[52] O. Romanets, L. Tolos, C. Garcia-Recio, J. Nieves, L. L. Salcedo and R. G. E. Timmermans, Phys. Rev. D **85**, 114032 (2012).
[53] C. Garcia-Recio, J. Nieves, O. Romanets, L. L. Salcedo and L. Tolos, Phys. Rev. D **87**, 074034 (2013).
[54] L. Tolos, Int. J. Mod. Phys. E **22**, 1330027 (2013).
[55] J. M. Torres-Rincon, L. Tolos and O. Romanets, Phys. Rev. D **89**, 074042 (2014).
[56] J. Adam *et al.* [ALICE Collaboration], arXiv:1509.06888 [nucl-ex].
[57] B. B. Abelev *et al.* [ALICE Collaboration], Phys. Rev. C **90**, 034904 (2014).
[58] S. K. Das, F. Scardina, S. Plumari and V. Greco, Phys. Lett. B **747**, 260 (2015).